buildings

MDPI

Article

Structural Comparison and Equivalent Design Method for Multi-Span Flexible Photovoltaic Supports in Mountainous Areas

Jinkang Diao [1,2], Yichen Zhao [3,*], Zhenyu Wang [3], Huajie Wang [3] and Feng Fan [2,*]

[1] Shanghai Electric Group Company Limited, Shanghai 200240, China
[2] School of Ocean Engineering, Harbin Institute of Technology at Weihai, Weihai 264209, China
[3] School of Civil Engineering, Harbin Institute of Technology, Harbin 150009, China
* Correspondence: zyc18645720195@163.com (Y.Z.); fanf@hit.edu.cn (F.F.)

Abstract

To address the problems of large terrain variation, limited foundation construction, and poor adaptability of conventional supports in mountain photovoltaic projects, this study establishes finite element models of four flexible photovoltaic support systems, including one single-layer cable system and three double-layer cable systems. Under the same span, module layout, and loading conditions, the deflection, cable force, support reaction, equivalent steel consumption, and torsional performance of the different systems are compared under symmetric and asymmetric loading. The results show that the single-layer cable system has the lowest material consumption and better constructability in mountain terrain, but its torsional stiffness is relatively weak. The double-layer systems provide better overall stiffness and torsional resistance, but require more steel and impose larger foundation reactions. The single-layer cable system is then selected for further analysis. To ensure geometric nonlinear convergence, the structural analysis relies on established catenary cable and beam element formulations under incremental loads. Based on the parameter analysis, a combination of 40° for the bottom ground cable and 50° for the top ground cable is recommended to reduce structural reaction moments. Finally, as a simplified structural analysis approach to avoid exhaustive global modeling, a two-span equivalent model for intermediate columns, a single-span equivalent model for edge columns, and a table-based selection procedure are proposed, providing a reference for the rapid design of mountain multi-span flexible photovoltaic supports.

Keywords: mountain photovoltaic; flexible support; cable structure; structural comparison; ground cable angle; equivalent design

Check for updates

Academic Editors: Eugeniusz Koda and Shaohong Cheng

Received: 8 May 2026
Revised: 27 June 2026
Accepted: 28 June 2026
Published: 9 July 2026

Copyright: © 2026 by the authors. Licensee MDPI, Basel, Switzerland. This article is an open access article distributed under the terms and conditions of the Creative Commons Attribution (CC BY) license.

1. Introduction

With the rapid expansion of solar power generation, the availability of suitable flat land for large-scale photovoltaic (PV) power plants has become increasingly limited. As a result, complex mountainous areas, hillsides, and barren slopes have gradually become important scenarios for PV development. Compared with conventional rigid supports, flexible PV supports that use prestressed cables or cable–strut systems as the main load-bearing components offer better terrain adaptability, longer spans, lower self-weight, and reduced foundation requirements, making them particularly suitable for irregular mountain terrains. Meanwhile, the long-term durability of PV materials, the service performance of supporting structures, and structural health monitoring under harsh environmental conditions have

received increasing attention [1–8]. These developments provide an important engineering basis for improving the reliability and applicability of flexible PV support systems in mountainous PV projects.

Among the loads acting on photovoltaic supports, wind load remains the primary controlling factor for structural safety and deformation control. For conventional photovoltaic systems, Jubayer and Hangan [9,10] conducted pioneering numerical simulations on stand-alone ground-mounted panels and panel arrays, establishing an early aerodynamic basis for evaluating wind effects on solar infrastructures. Kopp et al. [11] further clarified the aerodynamic mechanisms governing tilted roof-mounted solar arrays, while Aly [12] emphasized the influence of geometric scale in wind-tunnel assessment. Subsequent studies extended the research scope from isolated or simplified configurations to practical operating conditions. Wind-pressure distributions under varying tilt angles and wind directions were investigated through combined experimental and numerical approaches [13], and wind loading on sun-tracking ground arrays was evaluated for large photovoltaic plants [14]. Experimental–computational stress assessment and hybrid pressure-integration/buffeting-analysis methods further improved the understanding of module response and multi-row tracker interference [15,16]. Together, these studies provide robust wind-resistant design references for rigid supports and tracking systems, but their stiffness assumptions and failure modes differ substantially from those of cable-supported flexible configurations.

Compared with rigid structures, continuous flexible photovoltaic supports rely heavily on prestressed cables, making their responses strongly nonlinear and sensitive to span length, cable force, structural configuration, and boundary constraints. Wind-induced vibration, shading effects, torsional response, and field-measured load transmission have therefore become key concerns in flexible or lightweight photovoltaic systems [17–19]. He et al. [20,21] investigated vibration suppression and mechanical behavior of suspension-cable-supported photovoltaic modules, demonstrating the distinctive deformation and dynamic response mechanisms of cable-supported layouts. To identify safety limits, Liu et al. [22] experimentally determined the critical wind velocity of a 33 m-span flexible support, while Xu et al. [23] examined wind-induced vibration characteristics of suspension-cable-supported modules. Instability mechanisms and failure criteria of large-span flexible PV arrays under severe wind actions were further established by Li et al. [24]. In addition, the effects of initial pretension, module tilt angle, and ground-anchor cable layout on wind-induced response have been systematically evaluated [25–27], and cable-truss array studies have proposed vibration-response and suppression strategies for flexible support systems [28].

More recent investigations have moved toward large-span, double-layer, cable-supported structures and complex-site applications. Zhou et al. [29,30] performed wind-load measurements and aeroelastic wind-tunnel tests on large-span flexible photovoltaic supports, revealing pronounced spatial vibration and multi-span coupling characteristics, while earlier solar-wing studies provided useful references for aerodynamic vibration of lightweight photovoltaic structures [31]. For mountain-based PV projects, terrain-induced flow distortion further amplifies non-uniform wind pressures and interference effects along continuous arrays [32,33]. Mechanically, these systems behave as tension-dominated prestressed cable structures, whose equilibrium configuration and load-transfer path require shape-finding theory and geometric nonlinear analysis [34,35]. General nonlinear cable formulations and flutter-performance studies provide additional theoretical support for evaluating flexible photovoltaic supports under coupled wind–structure interaction [36–38].

Although previous studies have clarified wind-load characteristics, vibration mechanisms, instability criteria, and key design parameters, a standardized and computationally efficient framework for macro-structural selection and rapid simplified design of contin-

uous multi-span flexible photovoltaic supports under mountainous constraints remains insufficiently developed.

In response to these issues, this paper focuses on structural selection and rapid design of mountain multi-span flexible photovoltaic supports. Finite element models of one single-layer cable system and three double-layer cable systems are established. Under the same span, module layout, boundary conditions, and loading system, the mid-span deflection, cable force, support reaction, equivalent steel consumption, and torsional performance of different structures are compared under symmetric and asymmetric loads. Based on the structural comparison, the single-layer cable system, which is more suitable for mountain conditions, is selected for further study. The influence of the bottom and top ground cable angles on the stress of the main cable, the stress of the ground cables, and the support reaction moment is then investigated. Finally, for continuous multi-span structures in mountain terrain, a two-span equivalent model for intermediate columns and a single-span equivalent model for edge columns are proposed. The complex multi-span system is simplified into typical local sub-models, and a rapid selection procedure for column sections and cable systems is developed. The results provide a reference for structural selection, parameter optimization, and equivalent engineering design of mountain flexible photovoltaic supports.

2. Structural Systems and Finite Element Modeling of Flexible Supports

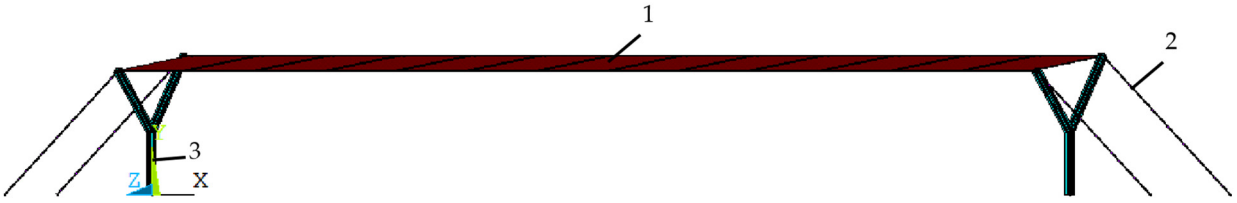
2.1. Structural Systems

To address the problems of large terrain variation, limited foundation construction, and poor adaptability of conventional rigid supports in mountain photovoltaic projects, four flexible photovoltaic support systems are constructed, including one single-layer cable system and three double-layer cable systems. Each system consists of photovoltaic modules, load-bearing cables, edge columns, struts, and stabilizing cables. The main differences among them lie in the number of cable types, the strut configuration, and the arrangement of stabilizing components. The single-layer cable system has a simple configuration and requires less space, while the double-layer cable systems improve structural stiffness and overall stability by adding secondary load-bearing units. To ensure comparability among the different systems, all schemes adopt the same span, module layout, boundary conditions, and loading system.

The four structural schemes demonstrate a clear evolution from component-level refinement to system-level integration (Figure 1). The single-layer cable structure (Structure Model 1) employs the simplest configuration—dual parallel load-bearing cables—offering direct force transfer and minimal steel consumption. The fish-belly double-layer structure (Structural Model 2) introduces lower stabilizing cables and vertical struts, utilizing the tension couple effect to significantly enhance torsional stiffness. The truss-type double-layer structure (Structural Model 3) replaces vertical struts with diagonal braces to form V-shaped units, balancing inter-layer forces through tension-compression coupling to optimize both stiffness and member efficiency. Finally, the three-load-bearing-cable double-layer structure (Structural Model 4) adopts an innovative single-row, three-cable layout. While increasing cable usage, it substantially reduces the number of perimeter columns and foundations via a unilateral load-bearing system, achieving a unified improvement in structural efficiency and economy, particularly suited for terrain-constrained mountainous sites.

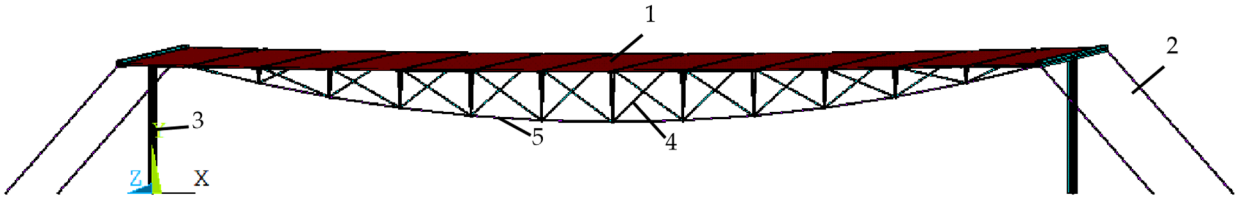
All four systems use load-bearing cables as the main structural members, forming a complete load transfer path through the edge columns and ground anchors. The single-layer system mainly relies on cable prestress to maintain its working shape, while the double-layer systems improve longitudinal stiffness and torsional resistance through cable–strut interaction. These systems cover typical mountain flexible support configurations

ranging from simple to complex, and can be used for subsequent comparison of mechanical behavior and structural selection.



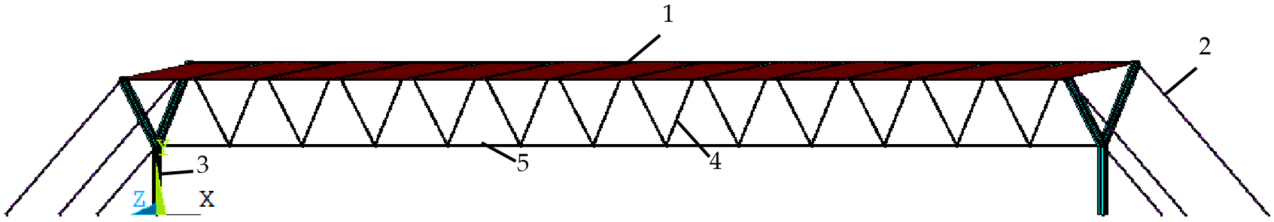
1 denotes the photovoltaic module; 2 denotes the load-bearing cable; 3 denotes the edge column.

(**a**) Single-layer cable structure (Structural Model 1).



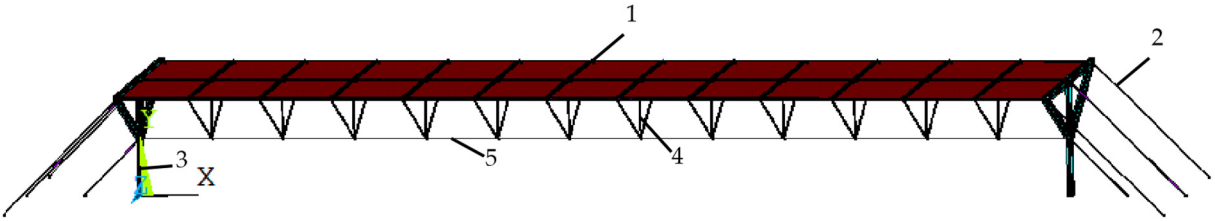
1 denotes the photovoltaic module; 2 denotes the load-bearing cable; 3 denotes the edge column; 4 denotes the strut; and 5 denotes the stabilizing cable.

(**b**) Fish-belly double-layer structure (Structural Model 2).



1 denotes the photovoltaic module; 2 denotes the load-bearing cable; 3 denotes the edge column; 4 denotes the strut; and 5 denotes the stabilizing cable.

(**c**) Truss-type double-layer structure (Structural Model 3).



1 denotes the photovoltaic module; 2 denotes the load-bearing cable; 3 denotes the edge column; 4 denotes the strut; and 5 denotes the stabilizing cable.

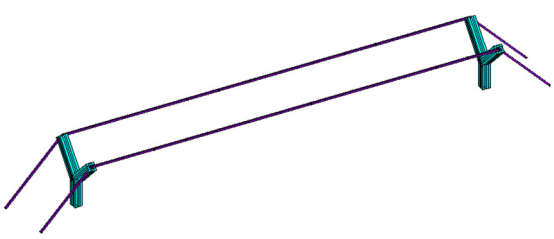
(**d**) Three-load-bearing-cable double-layer structure (Structural Model 4).

Figure 1. Schematic diagram of structural schemes.

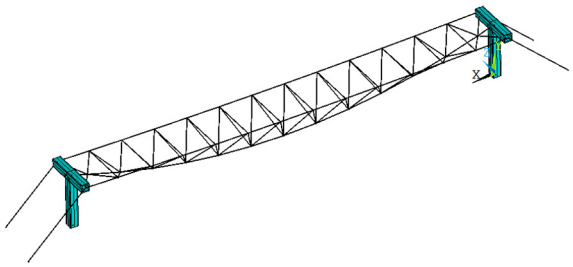
2.2. Model Parameters and Modeling Method

As shown in Figure 2, the four structures adopt the same geometric parameters to eliminate the influence of non-key factors. The span is 16 m. Photovoltaic modules are arranged uniformly along the span, with a module spacing of 0.0977 m. The spacing between the two load-bearing cables is 2 m, and their horizontal projection distance is 2.0147 m. Their heights above the ground are 2.217 m and 1.974 m, respectively, and the cable diameter is 15.2 mm. Each photovoltaic module weighs 25 kg and has dimensions of 2278 mm × 1133 mm. The modules are fixed to the two load-bearing cables along the long side by clamps. Tie rods are used at both ends to connect the structure to ground anchors. In terms of materials, the load-bearing cables are 1860 MPa prestressed steel strands, the

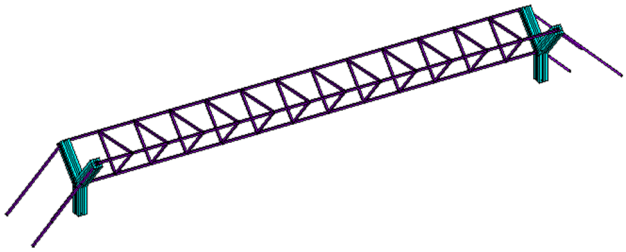
edge columns use box sections, and the inter-cable supports are treated as rigid members, the structural geometric and material parameters are presented in Table 1.



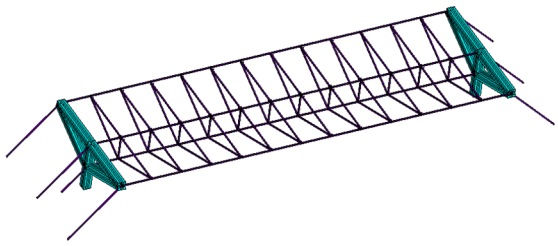
(**a**) Structural configuration of Model 1.



(**b**) Structural configuration of Model 2.



(**c**) Structural configuration of Model 3.



(**d**) Structural configuration of Model 4.

Figure 2. Schematic diagram of structural member arrangement without PV panels.

Table 1. Geometric and material parameters.

Member	Area/m^2	Elastic Modulus/GPa	Poisson's Ratio	Density/kg·m^{-3}	Thermal Expansion Coefficient	Design Parameter
Beam	8.4×10^{-3}	210	0.3	7850	1.2×10^{-5}	Box section
Column	8.4×10^{-3}	210	0.3	7850	1.2×10^{-5}	Box section
Strut	1.1×10^{-3}	210	0.3	7850	1.2×10^{-5}	Circular hollow section
Photovoltaic module	2.581	55	0.2	1927	1×10^{-6}	—
Steel cable	2.5×10^{-4}	190	0.3	7850	1.2×10^{-5}	—

Finite element analysis is carried out using the commercial finite element software ANSYS 2022R1. The load-bearing cables and stabilizing cables are modeled with tension-only LINK180 truss elements, which are set to carry tension only. The inter-cable supports are also modeled with LINK180 elements to represent rigid strut behavior. The edge columns are modeled with the 3D linear BEAM188 beam elements to capture bending and compression–bending behavior. The column bases are fixed to the ground. The ground-anchor nodes are restrained in all three translational degrees of freedom, and the connections between cables and support members are treated as hinged. Prestress is introduced by adjusting the temperature of the cables. Geometrically nonlinear static analysis is solved using the Newton-Raphson iteration method combined with the arc-length method. By setting the substep size to refine the load increment gradient and adopting an adaptive solution control strategy, the number of equilibrium iterations and convergence tolerance are automatically adjusted. Displacement- and load-based dual convergence criteria are employed to ensure computational stability and accuracy. This modeling approach can reflect the cooperative behavior and geometric nonlinearity of cables, struts, and columns in flexible supports, providing a consistent basis for comparing different structural systems. It should be noted that, for cable structures of this type, the

mesh discretization is not an arbitrary numerical refinement but is physically determined by the structural configuration: each cable segment between two adjacent physical connection points (e.g., column-top joints, ground anchors, cable-clamp nodes, and inter-cable strut intersections) constitutes a single LINK180 element. This element density faithfully captures the dominant load-transfer path of each cable segment. Artificially inserting intermediate nodes between physical connection points would introduce unconstrained degrees of freedom that lack physical stiffness, readily triggering spurious local buckling modes in the tension-only formulation and causing severe non-convergence in the Newton–Raphson iteration. Therefore, mesh refinement is neither required nor appropriate for the present class of flexible cable-supported structures, and the discretization adopted herein provides mesh-independent results by construction.

The structural modeling and nonlinear solver configurations in this study adhere strictly to standard computational mechanics procedures for cable-supported systems. The tension-only LINK180 elements and BEAM188 formulations are used within their mathematically verified load-bearing regimes. By utilizing the automated Newton-Raphson iteration combined with arc-length adjustment and multi-substep gradient refinement, the solver automatically filters out non-converging geometric nonlinear solutions. The consistent application of these standard computational controls guarantees the mathematical stability and internal algorithmic consistency of the relative trends presented in the subsequent comparative analysis.

2.3. Loads and Load Cases

Loads are transferred to the load-bearing cables through the photovoltaic modules. To reflect the actual load transfer path, wind and snow loads are converted into concentrated loads applied at the nodes of the load-bearing cables. The snow load is taken as 0.3 kN/m^2, and the basic wind pressure is taken as 0.65 kN/m^2. The wind load shape coefficient, gust response factor, and height variation coefficient of wind pressure are determined according to relevant codes. Considering that flexible supports may experience both uniform loading and partial loading under wind action, the load cases are divided into symmetric and asymmetric loading. The former is used to evaluate overall stiffness, cable force level, and material consumption, while the latter is used to describe the torsional response and stability performance caused by uneven loading on the two load-bearing cables. The load application diagram is illustrated in Figure 3.

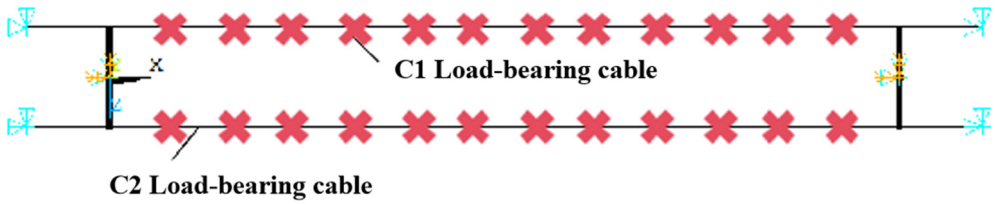


Figure 3. Load application diagram.

The load combinations are determined for both serviceability and ultimate limit states, considering dead load, positive wind pressure, wind suction, and snow load to satisfy deformation control and load-bearing safety requirements. The unified load application method and load case classification provide the basis for subsequent comparison of different structural systems and key parameter analysis. Table 2 presents the load combination factors used in the subsequent analyses.

Load determination strictly adheres to the Code for Structural Design of Photovoltaic Supports (NB/T 10115—2018) [39] and the Code for Structural Design of Flexible Photovoltaic Supports (T/CSEE 0394—2023) [40]. The calculation incorporates the wind

load shape coefficient, gust response factor, and height variation factor. Based on the wind-receiving area of the modules and the design wind speed, the parameters listed in Tables 3 and 4 were established. To simulate diverse loading states, symmetric load cases, defined by the shape coefficients in T/CSEE 0394—2023, characterize uniform wind action across the structure, whereas asymmetric load cases, based on NB/T 10115—2018, simulate complex states of non-uniform wind distribution.

Table 2. Load combination factors.

Load Combination	Dead Load	Positive Wind Pressure	Wind Suction	Snow Load
ZJ1	1.0	1.0	—	1.0
ZJ2	1.0	—	1.0	1.0
CJ1	1.3	1.5	—	1.5
CJ2	1.0	—	1.5	1.5

Note: ZJ denotes the serviceability limit state; CJ denotes the ultimate limit state.

Table 3. Wind load calculation parameters (Structure 1).

Parameter Type	Asymmetric Load				Symmetric Load	
	Wind Pressure		Wind Suction		Wind Pressure	Wind Suction
Basic wind pressure/kN·m^{-2}	0.65	0.65	0.65	0.65	0.65	0.65
Gust response factor	1.2	1.2	1.2	1.2	1.2	1.2
Wind load shape coefficient	0.66	0.18	−1.0	−0.34	0.8	−0.95
Wind pressure height variation factor	1.17	1.17	1.17	1.17	1.17	1.17
Standard wind pressure/kN·m^{-2}	0.603	0.165	0.913	0.311	0.73	0.87
PV panel area/m^2	2.581	2.581	2.581	2.581	2.581	2.581
Total wind force/kN	1.557	0.426	2.357	0.803	1.88	2.24

Table 4. Wind load calculation parameters (Structures 2, 3, 4).

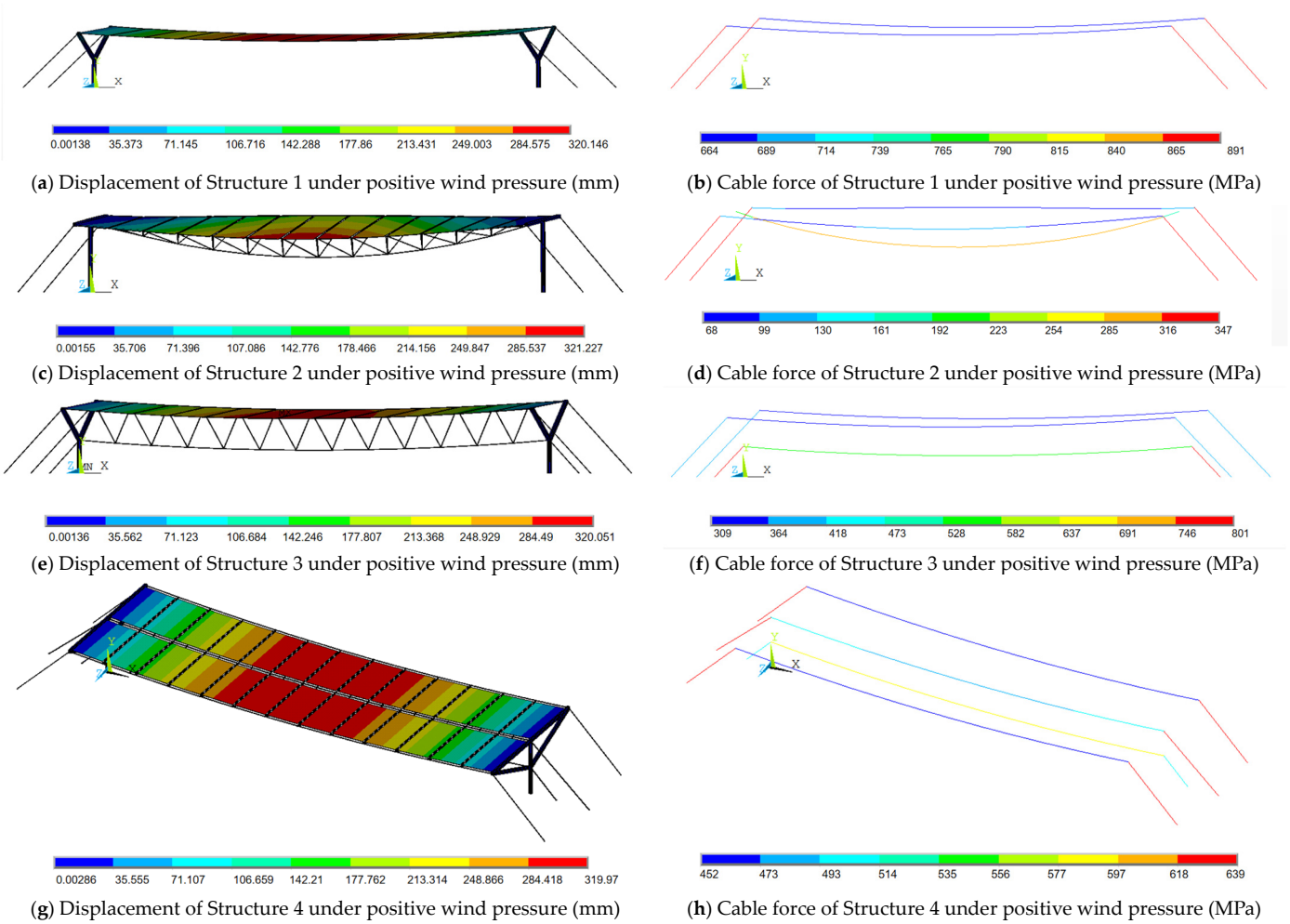
Parameter Type	Asymmetric Load				Symmetric Load	
	Wind Pressure		Wind Suction		Wind Pressure	Wind Suction
Basic wind pressure/kN·m^{-2}	0.65	0.65	0.65	0.65	0.65	0.65
Gust response factor	1.6	1.6	1.6	1.6	1.6	1.6
Wind load shape coefficient	0.66	0.18	−1.0	−0.34	0.8	−0.95
Wind pressure height variation factor	1.17	1.17	1.17	1.17	1.17	1.17
Standard wind pressure/kN·m^{-2}	0.804	0.221	1.218	0.415	0.98	1.16
PV panel area/m^2	2.581	2.581	2.581	2.581	2.581	2.581
Total wind force/kN	2.076	0.568	3.143	1.071	2.53	2.99

3. Comparative Analysis of Mechanical Performance of Different Systems

3.1. Comparison Under Symmetric Loading

In accordance with the design recommendations specified in the Code for Structural Design of Flexible Photovoltaic Supports (T/CSEE 0394—2023) [40], the deflection limit for

this design is set to L/50. Under symmetric loading, the structural responses of the different systems are mainly reflected in overall vertical stiffness, cable force level, support reaction, and material consumption. To ensure a consistent basis for comparison, the mid-span deflection serves as the primary metric. The required prestress, maximum cable stress, support reaction, and equivalent steel consumption per unit area of the four systems are compared under the same deformation requirement. This approach can objectively reflect the mechanical efficiency and economy of different structural systems under the same serviceability condition. Finite element analyses were conducted on the four structural configurations proposed earlier. The resulting responses under symmetric loading and positive wind pressure are presented in Figure 4.



(**a**) Displacement of Structure 1 under positive wind pressure (mm)

(**b**) Cable force of Structure 1 under positive wind pressure (MPa)

(**c**) Displacement of Structure 2 under positive wind pressure (mm)

(**d**) Cable force of Structure 2 under positive wind pressure (MPa)

(**e**) Displacement of Structure 3 under positive wind pressure (mm)

(**f**) Cable force of Structure 3 under positive wind pressure (MPa)

(**g**) Displacement of Structure 4 under positive wind pressure (mm)

(**h**) Cable force of Structure 4 under positive wind pressure (MPa)

Figure 4. Calculation results under symmetric loading and positive wind pressure.

The results under wind pressure, summarized in Tables 5 and 6, exhibit clear differences among the structures when they satisfy the same mid-span deflection requirement. Structure 1 has the lowest equivalent steel consumption per unit area, indicating that the single-layer cable system has a clear advantage in material efficiency. However, its required prestress in the load-bearing cables is much higher than that of the other systems, which means that this system relies more heavily on initial cable force to meet the stiffness target. Structure 2 has the lowest prestress level and relatively small support reactions, showing good longitudinal stiffness and load distribution capacity, but it has the largest steel consumption and is therefore less economical. Structure 3 is at an intermediate level in both prestress and steel consumption, showing a relatively balanced response. Structure 4 has higher support reactions and a larger amount of strut material, indicating that its

stiffness improvement is achieved through a stronger structural configuration, while also increasing the demand on foundations and material input.

Table 5. Results under positive wind pressure (symmetric loading).

Structure	Mid-Span Deflection/m	Prestress in Load-Bearing Cable/kN	Maximum Cable Stress/MPa	Cable Weight/kg	Strut Weight/kg	Support Reaction/kN	Equivalent Steel Consumption/kg·m^{-2}
1	0.32	127.792	696	62.4677	0	264.92	6.83
2	0.32	22.932	306	97.492	148.752	112.19	15.31
3	0.32	54.488	565	96.476	92.0853	263.29	13.4
4	0.32	94.120	667	118.94	313.55	471.99	11.404

Table 6. Results under wind suction (symmetric loading).

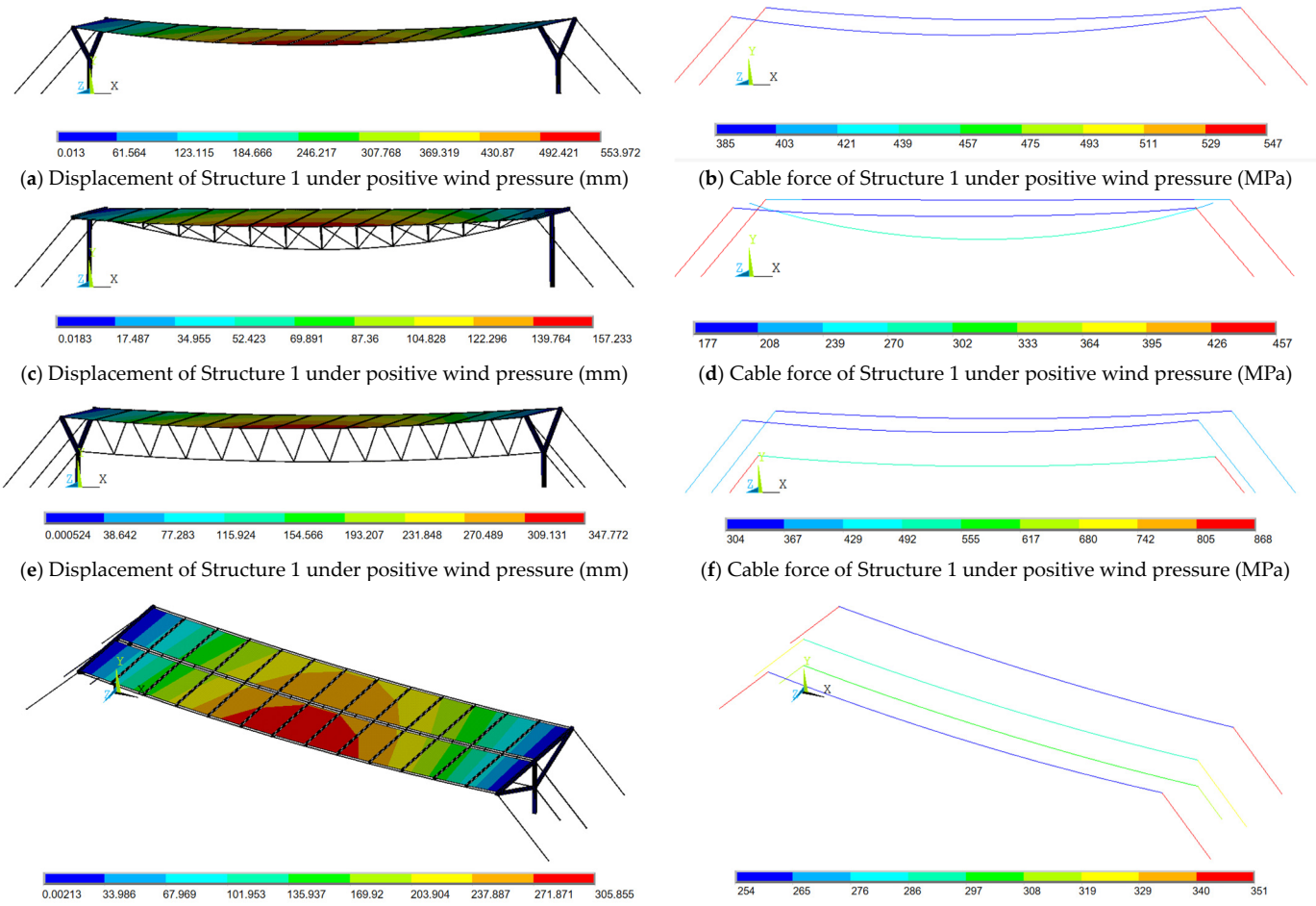
Structure	Mid-Span Deflection/m	Prestress in Load-Bearing Cable/kN	Maximum Cable Stress/MPa	Cable Weight/kg	Strut Weight/kg	Support Reaction/kN	Equivalent Steel Consumption/kg·m^{-2}
1	0.32	36.064	271	62.468	0	90.61	6.83
2	0.32	50.764	310	97.492	148.752	114.44	15.31
3	0.32	14.112	239	96.476	92.0853	99.72	13.4
4	0.32	22.625	266	118.94	313.55	156.72	11.404

Under wind suction, the relative trends among the structures are generally consistent with those under positive wind pressure, but their adaptability to load direction changes differs. For Structure 1, the prestress and cable stress decrease significantly under wind suction, indicating that the single-layer cable system experiences a more moderate stress state in this case while still maintaining low equivalent steel consumption. Structure 2 still shows high stiffness under wind suction, but its high steel consumption remains unchanged. Structure 3 has relatively low prestress and support reactions under wind suction, suggesting favorable longitudinal load-bearing behavior in this condition. Structure 4 remains stable overall under wind suction, but its support reactions are still relatively high, indicating that its stiffness advantage comes with higher foundation demand.

Overall, the structures show a clear trade-off between stiffness and economy under symmetric loading. The single-layer cable system achieves the lowest material consumption with fewer components, but it is more sensitive to the initial cable force. The double-layer systems improve stiffness through additional supports and stabilizing components, but generally increase material consumption and support reactions. For practical mountain photovoltaic applications, the symmetric-load analysis shows that Structure 1 has a strong economic advantage, while Structures 2 and 4 perform better in stiffness control.

3.2. Comparison Under Asymmetric Loading

Unlike symmetric loading, asymmetric loading causes the two load-bearing cables to carry different forces. The structure not only undergoes vertical deformation, but also develops a clear relative torsional response. Therefore, the comparison under asymmetric loading focuses on torsional performance and overall stability rather than only longitudinal stiffness. To maintain consistent comparison conditions, the prestress of the load-bearing cables is set to 50 kN for all structures. The mid-span relative rotation, mid-span deflection, maximum cable stress, and support reaction are used to evaluate the response of different systems under partial loading. The mid-span relative rotation is represented by the ratio of the maximum displacement difference between the two load-bearing cables at mid-span to the cable spacing and is used to describe the torsional stiffness of the structure.The calculation results under asymmetric loading are shown in Figure 5.



(**a**) Displacement of Structure 1 under positive wind pressure (mm)

(**b**) Cable force of Structure 1 under positive wind pressure (MPa)

(**c**) Displacement of Structure 1 under positive wind pressure (mm)

(**d**) Cable force of Structure 1 under positive wind pressure (MPa)

(**e**) Displacement of Structure 1 under positive wind pressure (mm)

(**f**) Cable force of Structure 1 under positive wind pressure (MPa)

(**g**) Displacement of Structure 1 under positive wind pressure (mm)

(**h**) Cable force of Structure 1 under positive wind pressure (MPa)

Figure 5. Calculation results under asymmetric loading and positive wind pressure.

Under positive wind pressure, Structure 1 has the largest mid-span relative rotation and mid-span deflection among the four schemes, indicating that the single-layer cable system has weak torsional resistance and insufficient overall stiffness under partial loading. Although it has the lowest cable weight and equivalent steel consumption, this economic advantage is achieved at the cost of larger deformation. Structure 2 has much smaller mid-span rotation and deflection than Structure 1, showing that the double-layer cable and support system is effective in limiting relative torsion caused by partial loading. Structure 3 has torsional response and deflection levels between those of Structures 1 and 2, showing a relatively balanced performance. Structure 4 has the smallest mid-span relative rotation and therefore the best torsional performance, but it also has the largest support reaction. This indicates that although Structure 4 can effectively restrain torsional deformation, it significantly increases foundation demand and structural complexity.

Under wind suction, the response trends of the four structures are generally similar to those under positive wind pressure (see Tables 7 and 8). Structure 1 still has the largest mid-span rotation and deflection and is the most sensitive to uneven loading. Structure 2 maintains good torsional performance, although its deformation control under wind suction is slightly weaker than under positive wind pressure. Structure 3 shows relatively small deflection and a stable cable stress distribution, indicating good load coordination under wind suction. Structure 4 still provides strong torsional resistance and small overall deformation, but its support reactions and structural complexity remain higher than those of the other schemes. These results show that under asymmetric loading, double-layer systems

are better able to adapt to the spatial effects caused by partial loading, and Structure 4 performs best in torsional control.

Table 7. Results under positive wind pressure (asymmetric loading).

Structure	Prestress in the Load-Bearing Cable/kN	Maximum Cable Stress /MPa	Mid-Span Relative Rotation	Cable Weight/kg	Strut Weight/kg	Support Reaction/kN	Mid-Span Deflection/m
1	50	547	0.095	62.4677	0	155.39	0.5539
2	50	457	0.031	97.492	148.752	143.45	0.1568
3	50	868	0.054	96.476	92.0853	249.49	0.3369
4	50	351	0.01532	118.94	313.55	375.95	0.3058

Table 8. Results under positive wind pressure (asymmetric loading).

Structure	Prestress in the Load-Bearing Cable/kN	Maximum Cable Stress /MPa	Mid-Span Relative Rotation	Cable Weight/kg	Strut Weight/kg	Support Reaction/kN	Mid-Span Deflection/m
1	50	419	0.102	62.468	0	155.39	0.553
2	50	392	0.068	97.492	148.752	107.04	0.320
3	50	718	0.049	96.476	92.0853	194.24	0.156
4	50	351	0.03647	118.94	313.55	280.44	0.18991

The asymmetric-load analysis further shows that differences among structural systems are reflected not only in longitudinal stiffness but also in their ability to adapt to uneven loading. The single-layer cable system is simple and economical, but has limitations in torsional control. The double-layer systems improve structural stability through spatial cooperative behavior and are more suitable for projects with strict deformation control requirements. Therefore, in the design of mountain flexible photovoltaic supports, the single-layer system may be preferred when material efficiency and construction simplicity are the main concerns, while the double-layer systems are more suitable when torsional response under partial loading needs to be controlled.

3.3. Comprehensive Evaluation and Structural Selection

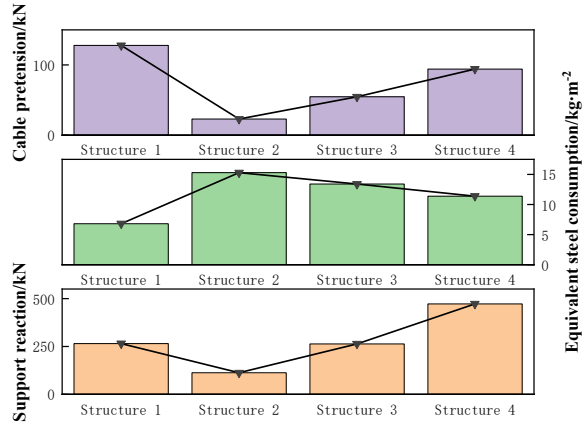
To evaluate the applicability of different structural systems in mountain terrain, it is necessary to consider both economy and longitudinal stiffness under symmetric loading, as well as torsional resistance and overall stability under asymmetric loading. According to the calculation results, Structure 1 has the greatest advantages in equivalent steel consumption per unit area and space requirement. It is simple in configuration and easy to construct, making it suitable for mountain sites with limited space and high economic requirements. Structure 2 performs well in both longitudinal stiffness and torsional resistance, but its material consumption is relatively high. Structure 3 shows relatively balanced performance, but does not have a clear advantage in any major indicator. Structure 4 has the best overall mechanical performance, especially in torsional stiffness, but its support reactions and structural complexity are high, requiring better foundation conditions and greater engineering investment.

Considering stiffness, torsional resistance, economy, and mountain-site adaptability, Structure 4 has the best overall performance from a purely mechanical point of view (see Table 9 and Figure 6). However, when practical constraints such as limited lower space, simplified construction, and construction convenience in mountain terrain are considered, Structure 1 is more suitable for engineering application. Therefore, the single-layer cable system is selected for subsequent analysis, with a focus on the optimization of key parameters such as the ground cable angle. This selection shows that the optimization of mountain

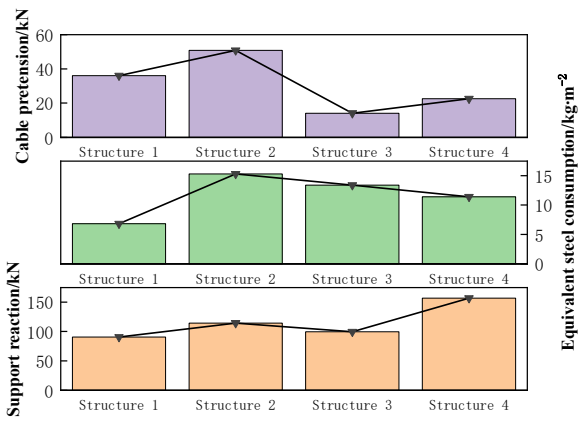
flexible photovoltaic supports should not pursue a single optimal mechanical index, but should balance structural performance, material consumption, and construction feasibility.

Table 9. Ranking of structural schemes.

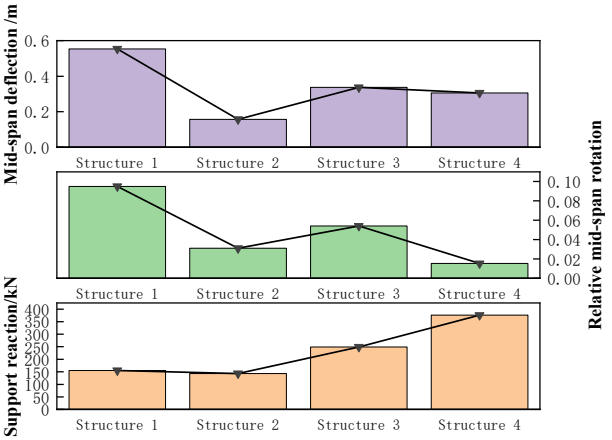
Structural Scheme	System Type	Space Requirement	Equivalent Steel Consumption	Longitudinal Stiffness	Torsional Stiffness	Overall Ranking
Structure 1	Single-layer	1	1	4	4	2.5
Structure 2		3	3	1	2	2.25
Structure 3	Double-layer	4	4	3	3	3.5
Structure 4		2	2	2	1	1.75



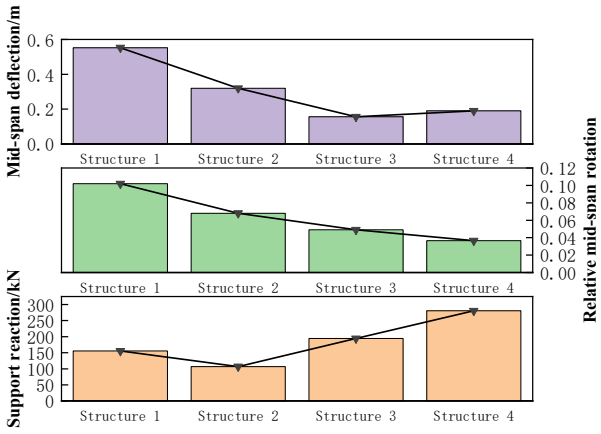
(**a**) Comparison of results under positive wind pressure (symmetric loading)



(**b**) Comparison of results under wind suction (symmetric loading)



(**c**) Comparison of results under positive wind pressure (asymmetric loading)



(**d**) Comparison of results under wind suction (asymmetric loading)

Figure 6. Comparison of calculation results.

4. Influence Mechanism and Optimization of Key Design Parameters

4.1. Parameter Selection and Evaluation Indices

Based on the structural comparison, the single-layer cable system is selected for further optimization because of its simple configuration, low material consumption, and better suitability for mountain terrain. The schematic diagram of the structural model parameters is shown in Figure 7. For this type of structure, load level, column height, and local terrain often vary with project conditions, while the arrangement of ground cables has more stable design significance. Therefore, the bottom and top ground cable angles are selected as the key parameters for analysis. The single-layer cable flexible support is used as the basic

model. Other geometric parameters remain unchanged, while the bottom and top ground cable angles are varied and combined with different mountain slope angles. Both wind load and snow load are taken as 0.3 kN/m^2 to represent typical mountain conditions.

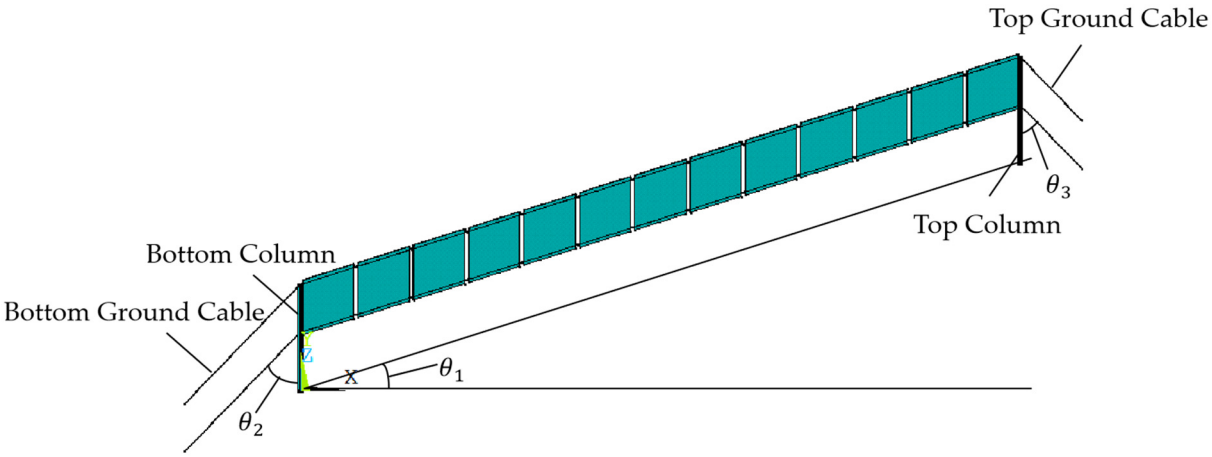


Figure 7. Analysis parameters and modeling of the single-layer cable system.

To reveal the influence of parameter changes on structural performance, the evaluation indices include the stress in the load-bearing cable, the stress in the bottom ground cable, the stress in the top ground cable, and the reaction moments at the bottom and top columns. The first three indices describe the internal force distribution of the cable system, while the last two reflect the force demand at the column and anchorage ends. This set of indices allows the influence of ground cable angle to be evaluated from both cable internal force and column reaction perspectives.

4.2. Influence of Ground Cable Angle on Cable-System Forces

The calculation results show that different cable members in the single-layer cable system have different sensitivities to the ground cable angles. The bottom ground cable angle mainly controls the primary load transfer path, while the top ground cable angle mainly affects the upper balancing path.

For the load-bearing cable, the stress generally decreases as the bottom ground cable angle increases, and this trend remains stable under different mountain slope angles. This indicates that when the direction of the bottom ground cable is closer to a favorable load transfer path, the additional tension carried by the main cable decreases and its stress state improves. As the mountain slope angle increases, the stress in the load-bearing cable increases slightly overall, but the controlling effect of the bottom ground cable angle does not change. By comparison, the top ground cable angle has a weaker effect on the load-bearing cable and mainly plays a local adjustment role.

As shown in Figure 8, the stress variation of cables in the single-layer flexible photovoltaic column exhibits a clear dependence on the ground cable angle and loading type. The stress in the bottom ground cable follows a trend similar to that of the load-bearing cable. It is also mainly controlled by the bottom ground cable angle and decreases clearly as the angle increases. When the bottom ground cable angle is small, the lower anchorage cable cannot effectively share the structural load, resulting in relatively high cable tension. As the angle increases, the force direction becomes more favorable and the internal force decreases. This shows that the bottom ground cable angle not only affects the working state of the main cable but also determines the force efficiency of the lower anchorage system.

The stress in the top ground cable is mainly controlled by the top ground cable angle and decreases as this angle increases. This is because an increased top ground cable angle

allows the upper anchorage cable to participate in overall equilibrium in a more favorable direction, thereby reducing the required cable tension. At the same time, there is a clear interaction between the upper and lower anchorage cables. When the bottom ground cable angle is relatively small, the top ground cable tends to take on more balancing force, leading to higher stress. Thus, although the two ground cables mainly control different parts of the system, they jointly determine the overall stress state of the single-layer cable structure.

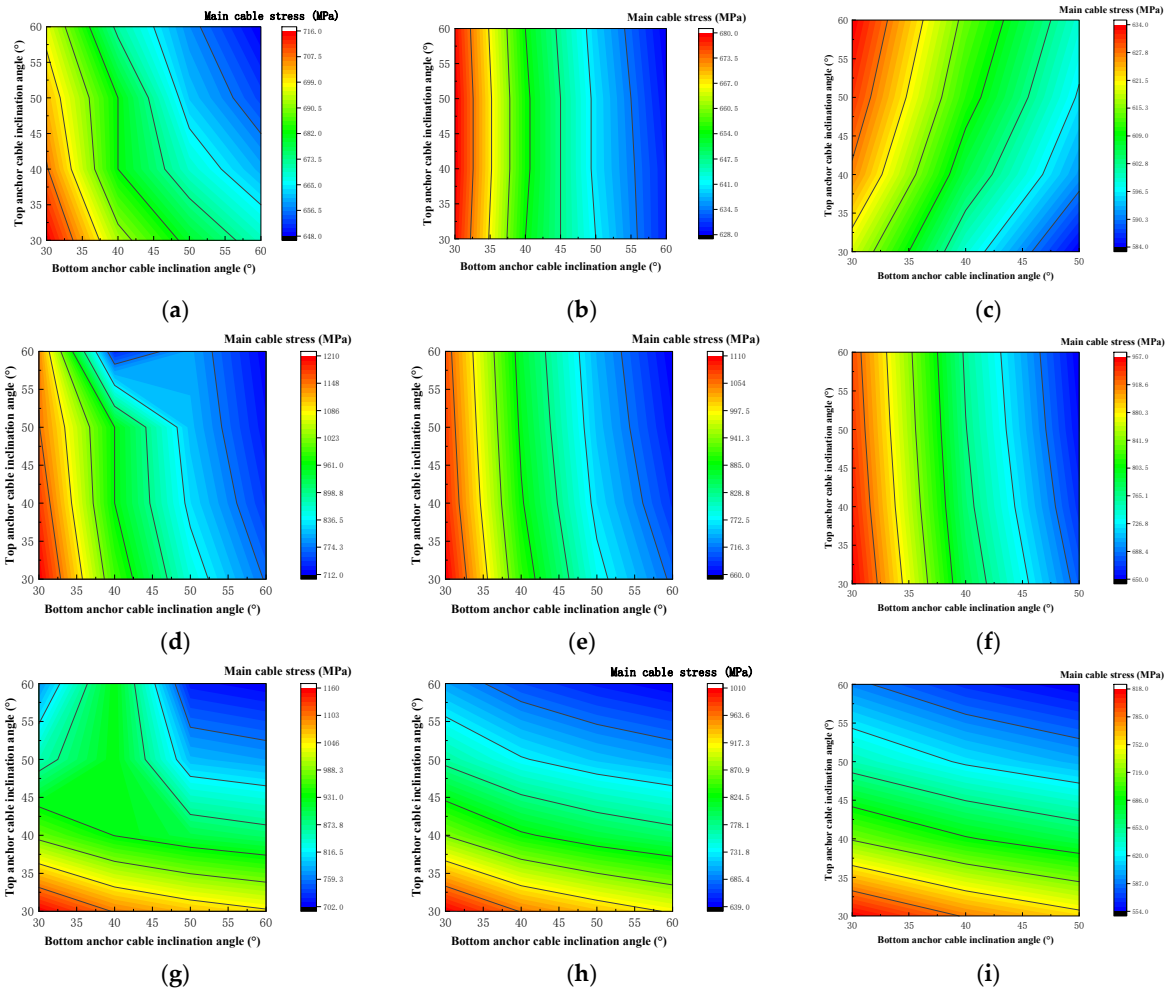


Figure 8. Stress variation of cables in the single-layer flexible photovoltaic column. (**a**) Stress distribution of the load-bearing cable (10°). (**b**) Stress distribution of the load-bearing cable (20°). (**c**) Stress distribution of the load-bearing cable (30°). (**d**) Stress distribution of the bottom ground cable (10°). (**e**) Stress distribution of the bottom ground cable (20°). (**f**) Stress distribution of the bottom ground cable (30°). (**g**) Stress distribution of the top ground cable (10°). (**h**) Stress distribution of the top ground cable (20°). (**i**) Stress distribution of the top ground cable (30°).

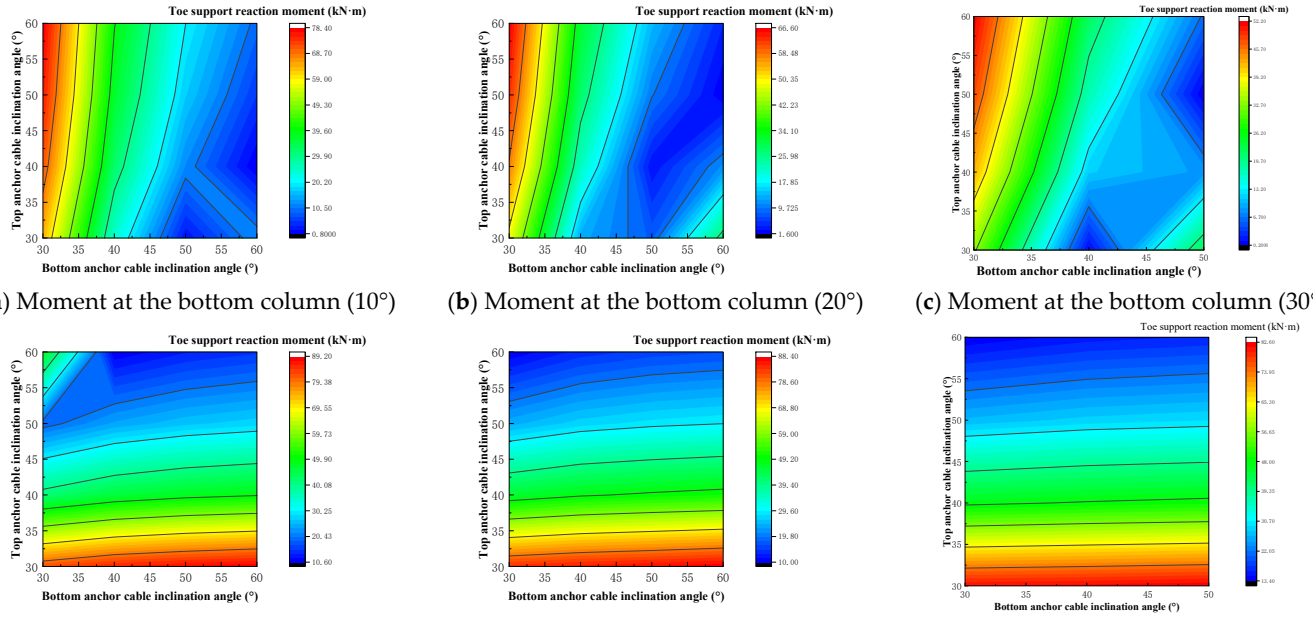
4.3. Influence of Ground Cable Angle on Support-System Forces

In addition to cable forces, the ground cable angle also has a significant influence on the support system, especially on the support reaction moment.

The reaction moment at the bottom column is mainly controlled by the bottom ground cable angle and decreases noticeably as this angle increases. The reaction moment at the top column is mainly controlled by the top ground cable angle and also shows a decreasing trend. The essential reason is that, as the ground cable angle increases, the anchorage cable force direction becomes closer to a reasonable load transfer path. The structural equilibrium is then achieved more through cable force decomposition, reducing the additional bending moment that must be carried at the column end. Therefore, optimizing the ground cable

angle not only improves the force state of the cable system but also reduces the constraint demand at the column base and anchorage end.

As shown in Figure 9, Combining the above results, the bottom ground cable angle mainly affects the load-bearing cable stress, bottom ground cable stress, and bottom column reaction moment, reflecting its control over the main load transfer path and the lower column system. The top ground cable angle mainly affects the top ground cable stress and top column reaction moment, reflecting its role in adjusting the upper anchorage system and the overall equilibrium state. The two angles act on different parts of the structure but jointly influence the structural behavior through overall force coupling.



(**a**) Moment at the bottom column (10°) (**b**) Moment at the bottom column (20°) (**c**) Moment at the bottom column (30°)

(**d**) Moment at the top column (10°) (**e**) Moment at the top column (20°) (**f**) Moment at the top column (30°)

Figure 9. Variation of column reaction moments in the single-layer flexible photovoltaic cable system.

4.4. Parameter Optimization and Design Recommendations

Based on the above results, appropriately increasing the ground cable angle helps reduce cable stress and column reaction moment, thereby improving the overall mechanical behavior of the single-layer cable system. However, a larger ground cable angle is not always better. As the angle increases, the anchorage cable becomes longer, and material consumption, tensioning difficulty, and anchorage layout requirements also increase. In mountain sites, an excessively large ground cable angle may also be limited by foundation conditions and available construction space. Therefore, parameter optimization should strike a balance among mechanical performance, constructability, and economy.

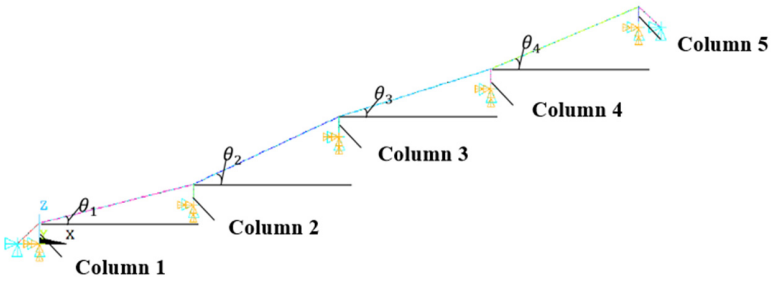
From the control relationship, the bottom ground cable angle should be prioritized for optimizing the load-bearing cable, the bottom ground cable, and the bottom column reaction. The top ground cable angle should be prioritized for optimizing the top ground cable and top column reaction. Under typical mountain slopes and loading conditions, a bottom ground cable angle of 40° and a top ground cable angle of 50° provide a good balance among cable force control, column reaction reduction, and construction feasibility. This parameter combination can therefore be used as a recommended design option for single-layer flexible photovoltaic supports. The result also shows that ground cable arrangement is one of the key design factors for single-layer cable systems and provides a unified parameter basis for later multi-span structural analysis.

5. Equivalent Simplified Design Method for Mountain Multi-Span Structures

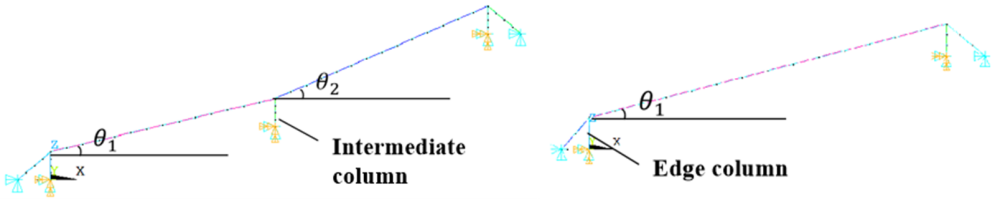
5.1. Multi-Span Structural Problem and Equivalent Model

In practical mountain photovoltaic projects, flexible supports are usually arranged as continuous multi-span systems. Compared with a single-span structure, a multi-span system is more strongly affected by terrain variation. Different spans may have different angles relative to the horizontal plane, leading to clear differences in geometry, load transfer paths, and column force states between adjacent spans. This is especially important for intermediate columns, which are often connected to two spans with different slopes. Edge columns are also controlled by boundary effects. If a refined model of the whole system is built and each span is designed separately, the number of parameter combinations becomes large and the calculation workload increases, which is not convenient for rapid engineering use.

For this reason, this paper proposes an equivalent simplified method for multi-span structures. The main idea is to retain the key geometric control parameters and main load transfer paths while dividing the overall multi-span model into typical local sub-models for analysis. The simplified model is shown in Figure 10. For intermediate columns, a two-span local equivalent model is used, with the angles of the two adjacent spans kept consistent with those in the original structure. For edge columns, a single-span local equivalent model is used, with the angle between the edge column and the adjacent span kept consistent with that in the original structure. In this way, the complex multi-span system can be converted into two typical problems: edge-column analysis and intermediate-column analysis. This significantly reduces modeling and computational complexity, and lays the foundation for later parametric selection and table-based engineering design.



(**a**) Four-span flexible photovoltaic support structure



(**b**) Equivalent model for the intermediate column (**c**) Equivalent model for the edge column

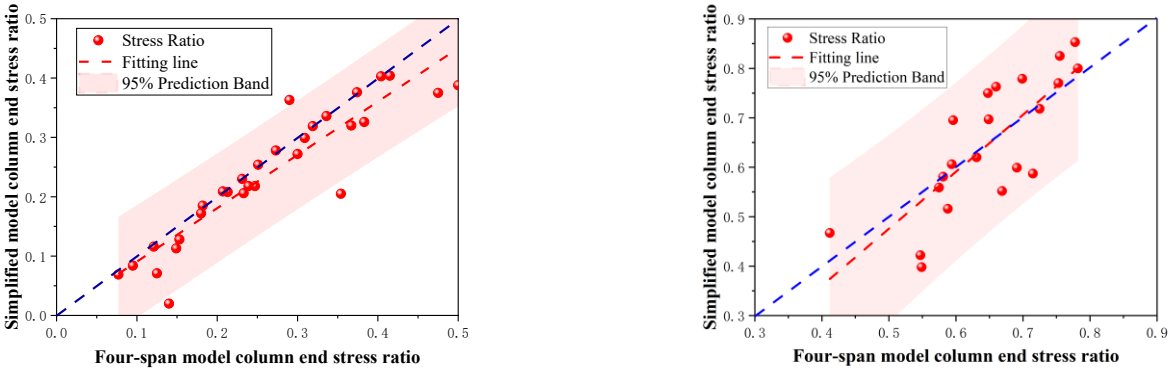
Figure 10. Equivalent models for mountain multi-span flexible photovoltaic supports.

5.2. Accuracy Verification and Applicability Analysis

To verify the reliability of the proposed equivalent simplified method, random angle combinations are used to generate refined four-span flexible photovoltaic support models. According to the principles described above, equivalent models for intermediate and edge columns are then established. The column-base reactions are extracted, and the stress ratios of the corresponding members before and after replacement are compared according to the stability check requirements for compression–bending members. The results show that the equivalent models agree well with those of the refined four-span

models. Most data points are concentrated within an acceptable error range, indicating that the method can reasonably reflect the force level of the main columns in multi-span flexible photovoltaic supports.

The results for intermediate columns are more concentrated, showing that their forces are mainly controlled by the angles of the two adjacent spans and that the equivalent model has relatively high accuracy. The results for edge columns are slightly more scattered, indicating that boundary members are more sensitive to overall boundary constraints and geometric asymmetry. Further analysis shows that the method has good applicability under both positive wind pressure and wind suction. Although the scatter of some points increases slightly under wind suction, the overall results remain within an acceptable engineering range. (see Figure 11). Therefore, the method is suitable for preliminary design and rapid selection of mountain multi-span flexible photovoltaic supports, especially for multi-scheme comparison and parametric analysis in small- and medium-sized projects.



(**a**) (**b**)

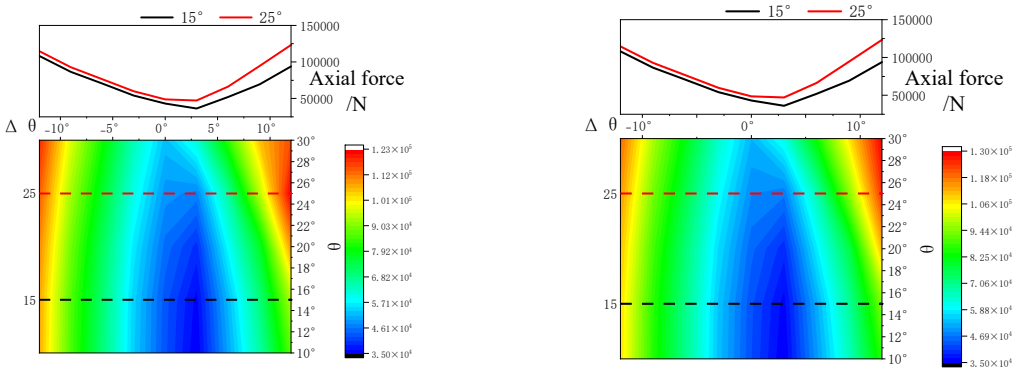
Figure 11. Comparison of replacement results. (**a**) Comparison of calculation results for intermediate columns under positive wind pressure. (**b**) Comparison of calculation results for intermediate columns under wind suction.

To further reveal the design applicability of the equivalent simplified method, this paper not only compares the stress ratios of the equivalent models and refined models, but also systematically analyzes the force patterns of the lower columns and upper cables. For intermediate columns, under a wind load of 0.3 kN/m^2 and a snow load of 0.3 kN/m^2, the variation of axial force and bending moment is shown in Figures 12 and 13. The results indicate that the maximum axial force usually occurs in regions with a large difference between the two span angles. When the angle difference is small, the structural force flow is more uniform and the axial force is lower. The bending moment reaches unfavorable values when both the span angle and the difference between the two span angles are large, showing that the geometric angle combination is a key factor influencing intermediate-column forces. Column height has a relatively limited effect on the axial force of intermediate columns, but it changes the bending moment level and should still be considered in section design.

For edge columns, the force pattern is shown in Figure 14. Both the axial force and bending moment of edge columns increase clearly with the single-span inclination angle, while the influence of column height is secondary. This suggests that the slope angle should be given priority in the design of edge columns.

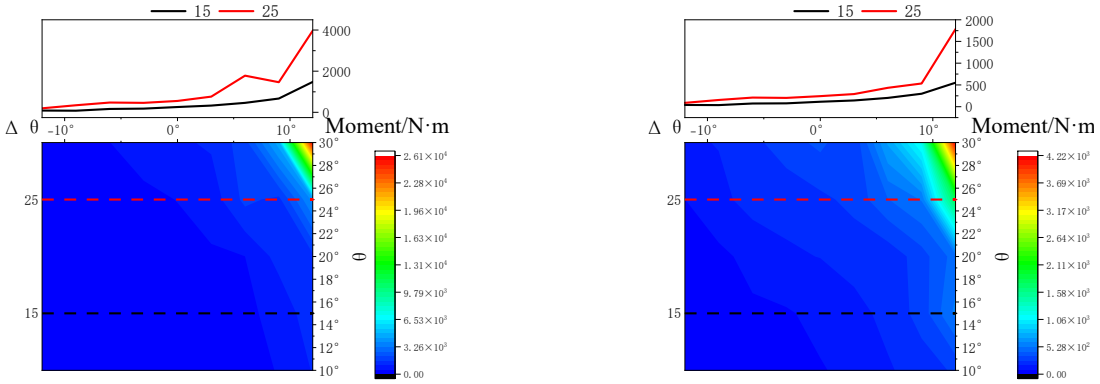
The engineering and practical value of the proposed equivalent sub-models lies in simplifying the preliminary analysis workflow for complex mountain flexible arrays. Continuous structures on irregular mountainous terrain typically require repetitive, full-scale modeling to account for variable adjacent slopes, which increases the computational workload during early-stage scheme comparison. By isolating the dominant local

parameters—specifically the angle differences for intermediate columns and inclination angles for edge columns—the proposed method transforms a globally variable spatial problem into standardized local configurations. The calibration results show that the structural response deviations remain within an acceptable engineering range of 12%. This demonstrates that the approach successfully reduces iterative modeling efforts while maintaining an adequate safety margin for conceptual design exploration.



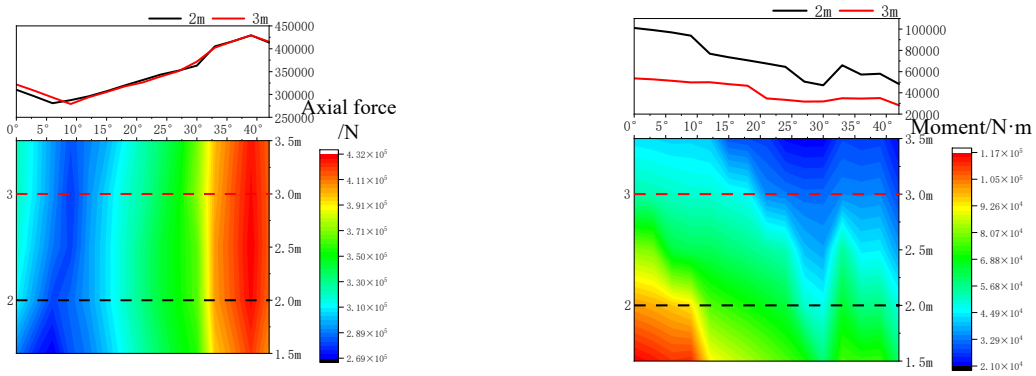
(**a**) Axial force diagram for a column height of 1.5 m (**b**) Axial force diagram for a column height of 2.5 m

Figure 12. Axial force of intermediate columns a under wind load of 0.3 kN/m^2 and a snow load of 0.3 kN/m^2.



(**a**) Bending moment diagram for a column height of 1.5 m (**b**) Bending moment diagram for a column height of 2.5 m

Figure 13. Bending moment of intermediate columns under a wind load of 0.3 kN/m^2 and a snow load of 0.3 kN/m^2.



(**a**) Calculation results of axial force for edge columns (**b**) Calculation results of bending moment for edge columns

Figure 14. Calculation results for edge columns under a wind load of 0.3 kN/m^2 and a snow load of 0.3 kN/m^2.

5.3. Application Boundaries of the Equivalent Method

To ensure structural safety and reliability in engineering practices, the precision benchmarks, geometric limitations, and restricted application zones of the proposed equivalent sub-models must be rigorously established. Through comprehensive parametric evaluations against the fully refined four-span models, the stress ratio discrepancies for intermediate columns are consistently maintained within plus or minus 5%, with internal forces exhibiting a maximum variance of plus or minus 8%. For edge columns, owing to their heightened sensitivity to localized boundary constraints, the peak structural response deviation is bounded within plus or minus 12% under critical wind suction loading conditions. These metrics strictly align with the standard engineering precision threshold of plus or minus 15% typically permitted during the preliminary planning and structural scheme comparative stages.

The structural safety of this equivalent approach is fundamentally constrained by defined topographical and loading envelopes. Specifically, the method is mathematically validated for multi-span systems possessing standard individual span lengths ranging from 15 m to 40 m, and individual slope inclinations not exceeding 35°. Furthermore, to control adverse geometric structural coupling between adjacent spans, the absolute slope angle difference between any two contiguous spans must be structurally restricted to $|\Delta\theta| \leq 15°$. Correspondingly, the basic operational environment should not exceed a basic wind pressure of 0.9 kN/m^2 and a snow load of 0.6 kN/m^2.

Consequently, specific engineering environments are explicitly excluded from this simplified framework to prevent severe structural underestimation. The sub-model methodology is prohibited in severe micro-topographies where local slope angle discrepancies abruptly exceed 20°, or in high-altitude terrain experiencing basic wind pressures greater than 1.0 kN/m^2 where aerostatic divergence and dynamic wind-induced vibrations dictate the design, necessitating full-scale time-history simulations.

5.4. Engineering Application

In engineering design, the rapid selection method for multi-span flexible photovoltaic supports is further organized into a workflow of "load zoning–column selection–cable selection." For the design of lower columns, the wind load and snow load of the project site are first used to consult Table 10 and determine the corresponding Supplementary Materials. For example, when the wind load is 0.3 kN/m^2 and the snow load is 0, Supplementary Materials SA is used; when the wind load is 0.6 kN/m^2 and the snow load is 0.3 kN/m^2, Supplementary Materials SE is used.

Table 10. Reference table for load regions.

Wind Load (kN/m^2)	Snow Load (kN/m^2)		
	0	**0.3**	**0.6**
0.3	Supplementary Materials SA	Supplementary Materials SD	Supplementary Materials SG
0.6	Supplementary Materials SB	Supplementary Materials SE	Supplementary Materials SH
0.9	Supplementary Materials SC	Supplementary Materials SF	Supplementary Materials SI

The corresponding selection table is then chosen according to the position of the column in the structure, specifically whether it is an intermediate column or an edge column. Taking Supplementary Materials SA as an example, intermediate columns can be selected from Supplementary Materials SA according to column height, and the section

number is determined by the single-span angle and the angle difference between two adjacent spans. Edge columns are selected using Supplementary Materials SA, where the recommended section is determined by column height and span inclination angle.

Type A sections are cold-formed thin-walled square steel tubes, and Type C sections are H-shaped steel sections. The corresponding geometric dimensions of each section are listed in Tables 11 and 12.

Table 11. Selection table for Type A sections.

Section No.	Dimensions/mm h	t	Area/cm^2	Unit Weight/(kg/m)	ix/cm	wx/cm^3
A1	60	2	4.64	3.87	2.37	8.68
A2	60	2.5	5.75	4.80	2.35	10.58
A3	80	2	6.24	5.21	3.19	15.83
A4	80	2.5	7.75	6.47	3.17	19.42
A5	100	2.5	9.75	8.13	3.98	30.92
A6	100	3	11.64	9.71	3.96	36.54
A7	120	2.5	11.75	9.80	4.80	45.08
A8	120	3	14.04	11.71	4.78	53.42
A9	140	3	16.44	13.71	5.59	73.50
A10	140	3.5	19.11	15.94	5.57	84.83
A11	140	4	21.76	18.15	5.55	95.91
A12	160	3.5	21.91	18.28	6.39	111.85
A13	160	4	24.96	20.82	6.37	126.63
A14	160	4.5	27.99	23.35	6.35	141.12
A15	160	5	31	25.86	6.33	155.32
A16	180	5	35	29.20	7.15	198.66
A17	200	5	39	32.53	7.96	247.33
A18	220	5	43	35.87	8.78	301.33
A19	240	6	56.16	46.85	9.56	427.38
A20	260	7	70.84	59.10	10.33	581.78
A21	280	7	76.44	63.77	11.15	678.66
A22	300	8	93.44	77.95	11.93	885.89

Table 12. Selection table for Type C sections.

Section No.	Dimensions				Area/cm^2	Unit Weight/(kg/m)
	$H \times B$	t1	t2	r		
C1	125 × 125	6	8	10	21.90	17.2
C2	150 × 150	7	10	13	40.55	31.9
C3	175 × 175	7.5	11	13	51.43	40.3
C4	200 × 200	8	12	16	72.28	56.7
C5	250 × 250	9	14	16	104.7	82.2
C6	250 × 255	14	14	16	104.7	82.2
C7	294 × 302	12	12	20	108.3	85.0
C8	300 × 300	10	15	20	120.4	94.5
C9	344 × 348	10	16	20	146.0	115

For the design of the upper cable system, the load level is again used to consult Table 13, the cable-structure selection reference table, and to determine the applicable Supplementary Materials range from Supplementary Materials SJ–SR. For example, Supplementary Materials SJ is applicable to the case with a wind load of 0.3 kN/m^2 and a snow load of 0, while Supplementary Materials SN corresponds to the case with a wind load of 0.6 kN/m^2 and a snow load of 0.3 kN/m^2.

Table 13. Reference table for cable-structure selection.

Wind Load (kN/m^2)	Snow Load (kN/m^2)		
	0	**0.3**	**0.6**
0.3	Supplementary Materials SJ	Supplementary Materials SM	Supplementary Materials SP
0.6	Supplementary Materials SK	Supplementary Materials SN	Supplementary Materials SQ
0.9	Supplementary Materials SL	Supplementary Materials SO	Supplementary Materials SR

After the load Supplementary Materials is determined, the corresponding cable selection table is consulted according to column height, single-span angle, and the angle difference between two adjacent spans. For example, Supplementary Materials SJ correspond to column heights from 1.5 m to 3.5 m, respectively, and provide recommended values for cable prestress and cable diameter. The tables give both the design prestress and the steel strand diameter. For instance, under a wind load of 0.3 kN/m^2, a snow load of 0, and a column height of 1.5 m, when the single-span angle is 10° and the angle difference between two spans is 0°, the recommended prestress is about 80 kN and the cable diameter is 15.2 mm. When the single-span angle increases to 30° and the angle difference between two spans increases to 12°, the prestress increases to 136 kN, while the cable diameter can still be 15.2 mm. This shows that the proposed method converts column section selection and cable prestress configuration, which would otherwise require repeated modeling and calculation, into a standardized table-based design process. It can therefore greatly improve the efficiency of scheme design and preliminary design for mountain multi-span flexible photovoltaic supports.

6. Conclusions

This paper investigates structural system comparison, key parameter optimization, and an equivalent simplified design method for mountain multi-span flexible photovoltaic supports. The main conclusions are as follows:

(1) Under symmetric loading, the different flexible support systems show a clear trade-off between stiffness and economy. The single-layer cable system has a simple configuration and the lowest equivalent steel consumption per unit area, giving it good economy and constructability in mountain terrain. However, its stiffness control depends more strongly on a relatively high initial prestress. The double-layer cable systems can improve overall vertical stiffness through cable–strut interaction, but this usually comes with higher material consumption and greater structural complexity.

(2) Under asymmetric loading, the differences among the structural systems are mainly reflected in torsional stiffness and overall stability. The single-layer cable system shows larger mid-span relative rotation and deflection under partial loading, indicating relatively weak torsional resistance. The double-layer cable systems can effectively limit the relative deformation between the two load-bearing cables. Among them, Structure 4 provides the best torsional performance, but it also leads to larger support reactions and higher structural cost.

(3) The ground cable angle is a key parameter affecting the mechanical performance of the single-layer flexible cable support. The bottom ground cable angle mainly controls the load-bearing cable stress, bottom ground cable stress, and bottom column reaction moment, while the top ground cable angle mainly affects the top ground cable stress and top column reaction moment. Increasing the ground cable angle within a reasonable range can reduce cable stress and column reaction moment, but an

excessively large angle increases cable length and construction difficulty. Considering both mechanical performance and constructability, a bottom ground cable angle of 40° and a top ground cable angle of 50° are recommended for typical mountain conditions.

(4) To improve the efficiency of refined modeling for mountain multi-span flexible photovoltaic supports, a two-span equivalent model for intermediate columns and a single-span equivalent model for edge columns are proposed. The structural simulation framework utilizes theoretically established geometric nonlinear formulations and standard convergence criteria to ensure numerical stability. Calibration against fully refined global models confirms that the structural column response deviations remain within an acceptable engineering range of 12%. This table-based design procedure is safely applicable to multi-span structures with standard single spans of 15–40 m, slope angles $\leq 35°$, and adjacent span angle differences $\leq 15°$, successfully transforming complex spatial multi-span calculations into a standardized analysis methodology for preliminary layout evaluation.

(5) Although the single-layer cable system offers superior economy, its weak torsional stiffness elevates risks of wind-induced flutter and aerostatic instability under severe wind suction. To mitigate these dynamic risks, structural safety must be governed by optimizing initial cable prestress and utilizing localized aerodynamic counterweights. In engineering designs, close attention must be paid to wind-induced resonant responses, and implementing auxiliary stabilizing cables or rigid cross-braces is highly recommended as the primary control measure for complex mountainous terrains.

Supplementary Materials: The following supporting information can be downloaded at: https://www.mdpi.com/article/10.3390/buildings16142721/s1.

Author Contributions: Conceptualization, J.D., Y.Z., Z.W., H.W. and F.F.; Methodology, J.D. and Y.Z.; Validation, Y.Z., Z.W., H.W. and F.F.; Investigation, J.D.; Resources, Y.Z.; Writing—original draft, J.D.; Writing—review & editing, J.D. and Y.Z.; Visualization, J.D., Y.Z., Z.W., H.W. and F.F.; Supervision, Y.Z. and H.W.; Funding acquisition, H.W. All authors have read and agreed to the published version of the manuscript.

Funding: This work was financially supported by the Scientific Research Funds of Shanghai Electric Power Generation Equipment Co., Ltd. (Grant No. 2024-Mountain Flexible Photovoltaic).

Data Availability Statement: Data are contained within the article.

Conflicts of Interest: Authors have received Funding from Scientific Research Funds of Shanghai Electric Power Generation Equipment Co., Ltd. Author Jinkang Diao was employed by the company Shanghai Electric Group Company Limited. The remaining authors declare that the research was conducted in the absence of any commercial or financial relationships that could be construed as a potential conflict of interest.

References

1. Barretta, C.; Oreski, G.; Feldbacher, S.; Resch-Fauster, K.; Pantani, R. Comparison of Degradation Behavior of Newly Developed Encapsulation Materials for Photovoltaic Applications. *Polymers* **2021**, *13*, 271. [CrossRef] [PubMed]
2. Dong, J.; Zhang, Z.; Yang, T.; Wang, J.; Ma, M.; Chen, W.; Wang, H.; Qian, H.; Fan, F. Comparative study on surface morphology evolution and mechanical property degradation of galvanized steel under different corrosion tests and its service life prediction. *Case Stud. Constr. Mater.* **2025**, *23*, e05242. [CrossRef]
3. Baiamonte, M.; Colletti, C.; Ragonesi, A.; Gerardi, C.; Dintcheva, N.T. Durability and Performance of Encapsulant Films for Bifacial Heterojunction Photovoltaic Modules. *Polymers* **2022**, *14*, 1052. [CrossRef] [PubMed]
4. Zang, Z.; Dong, J.; Ma, M.; Chen, W.; Wang, H.; Qian, H.; Fan, F. The aging behavior and failure mechanism of epoxy-acrylic polyurethane coating system under different accelerated testing methods. *Eng. Fail. Anal.* **2026**, *188*, 110650. [CrossRef]
5. Lou, Y.; Zhang, J.; Pan, Y. Static and Dynamic Response Analysis of Flexible Photovoltaic Mounts. *Buildings* **2024**, *14*, 2037. [CrossRef]

6. Chen, W.; Zhang, Z.; Wang, H.; Qian, H.; Feng, H.; Qiu, J.; Chen, S.; Chen, H.; Fan, F. Study on the compressive load-bearing capacity of corroded angle steel with single-sided connected. *Eng. Struct.* **2025**, *342*, 120840. [CrossRef]
7. Di, Z.; Wang, F.; Yu, H.; Dai, X.; Luo, B.; Liu, X. Analytical Formulation and Optimization of the Initial Morphology of Double-Layer Cable Truss Flexible Photovoltaic Supports. *Buildings* **2024**, *14*, 2549. [CrossRef]
8. Wang, Y.; Shi, Y.; Yang, T.Y. Structural Performance Warning Based on Computer Intelligent Monitoring and Fractional-Order Multi-Rate Kalman Fusion Method. *Fractal Fract.* **2026**, *10*, 186. [CrossRef]
9. Jubayer, C.M.; Hangan, H. Numerical Simulation of Wind Effects on a Stand-Alone Ground Mounted Photovoltaic (PV) System. *J. Wind Eng. Ind. Aerodyn.* **2014**, *134*, 56–64. [CrossRef]
10. Jubayer, C.M.; Hangan, H. A Numerical Approach to the Investigation of Wind Loading on an Array of Ground Mounted Solar Photovoltaic (PV) Panels. *J. Wind Eng. Ind. Aerodyn.* **2016**, *153*, 60–70. [CrossRef]
11. Kopp, G.A.; Farquhar, S.; Morrison, M.J. Aerodynamic Mechanisms for Wind Loads on Tilted, Roof-Mounted, Solar Arrays. *J. Wind Eng. Ind. Aerodyn.* **2012**, *111*, 40–52. [CrossRef]
12. Aly, A.M. On the Evaluation of Wind Loads on Solar Panels: The Scale Issue. *Sol. Energy* **2016**, *135*, 423–434. [CrossRef]
13. Yemenici, O.; Aksoy, M.O. An Experimental and Numerical Study of Wind Effects on a Ground-Mounted Solar Panel at Different Panel Tilt Angles. *J. Wind Eng. Ind. Aerodyn.* **2021**, *213*, 104630. [CrossRef]
14. Reina, G.P.; De Stefano, G. Computational Evaluation of Wind Loads on Sun-Tracking Ground-Mounted Photovoltaic Panel Arrays. *J. Wind Eng. Ind. Aerodyn.* **2017**, *170*, 283–293. [CrossRef]
15. Wittwer, A.R.; Podestá, J.M.; Castro, H.G.; Mroginski, J.L.; Marighetti, J.O.; De Bortoli, M.E.; Paz, R.R.; Mateo, F. Wind Loading and Its Effects on Photovoltaic Modules: An Experimental–Computational Study. *Sol. Energy* **2022**, *240*, 315–328. [CrossRef]
16. Taylor, Z.J.; Browne, M.T.L. Hybrid Pressure Integration and Buffeting Analysis for Multi-Row Wind Loading in an Array of Single-Axis Trackers. *J. Wind Eng. Ind. Aerodyn.* **2020**, *197*, 104056. [CrossRef]
17. Zhang, Z.; Xiao, Z.; Ma, W.; Liu, X. Wind-Induced Vibration Characteristics and Shading Effects of a Double-Layer Cable-Supported Photovoltaic Module System. *Buildings* **2025**, *15*, 550. [CrossRef]
18. Zhang, X.; Ma, W.; Zhang, Z.; Hu, L.; Cui, Y. Experimental Experimental Study on the Interference Effect of the Wind-Induced Large Torsional Vibration of Tracker Arrays. *J. Wind Eng. Ind. Aerodyn.* **2023**, *240*, 105470. [CrossRef]
19. Koekemoer, J.H.; Bredell, J.R.; Venter, G.; Reinecke, J. Field Measurements of Wind Load Effects in a Photovoltaic Single-Axis Tracker Mounting Rail. *J. Wind Eng. Ind. Aerodyn.* **2024**, *253*, 105876. [CrossRef]
20. He, X.-H.; Ding, H.; Jing, H.-Q.; Zhang, F.; Wu, X.-P.; Weng, X.-J. Wind-induced Vibration and Its Suppression of Photovoltaic Modules Supported by Suspension Cables. *J. Wind Eng. Ind. Aerodyn.* **2020**, *206*, 104275. [CrossRef]
21. He, X.-H.; Ding, H.; Jing, H.-Q.; Wu, X.-P.; Weng, X.-J. Mechanical Characteristics of a New Type of Cable-Supported Photovoltaic Module System. *Sol. Energy* **2021**, *226*, 408–420. [CrossRef]
22. Liu, J.; Li, S.; Luo, J.; Chen, Z. Experimental Study on Critical Wind Velocity of a 33-Meter-Span Flexible Photovoltaic Support Structure. *J. Wind Eng. Ind. Aerodyn.* **2023**, *236*, 105355. [CrossRef]
23. Xu, H.; Ding, K.; Shen, G.; Du, H.; Chen, Y. Experimental Investigation on Wind-Induced Vibration of Photovoltaic Modules Supported by Suspension Cables. *Eng. Struct.* **2024**, *299*, 117125. [CrossRef]
24. Li, W.; Ke, S.; Cai, Z.; Ji, C.; Wang, W.; Wang, L.; Ren, H. Instability Mechanism and Failure Criteria of Large-Span Flexible PV Support Arrays under Severe Wind. *Sol. Energy* **2023**, *264*, 112000. [CrossRef]
25. Zhu, Y.F.; Huang, Y.; Guo, Y.; Xiao, B.; Chen, C.H.; Yao, Y. Numerical Assessment of the Initial Pre-Tension Impact on Wind-Induced Vibration in Flexible Cable-Supported Photovoltaic Systems. *J. Wind Eng. Ind. Aerodyn.* **2024**, *251*, 105788. [CrossRef]
26. Zhu, Y.F.; Huang, Y.; Xu, C.; Xiao, B.; Chen, C.H.; Yao, Y. Effect of Tilt Angle on Wind-Induced Vibration in Pre-Stressed Flexible Cable-Supported Photovoltaic Systems. *Sol. Energy* **2024**, *277*, 112729. [CrossRef]
27. Zhu, Y.F.; Huang, Y.; Xu, C.; Xiao, B.; Chen, C.H.; Yao, Y. Analysis of Wind-Induced Vibration Effect Parameters in Flexible Cable-Supported Photovoltaic Systems. *Case Stud. Constr. Mater.* **2024**, *20*, e03368. [CrossRef]
28. Wu, Y.; Wu, Y.; Sun, Y.; Sun, X. Wind-Induced Vibration Response and Suppression of the Cable-Truss Flexible Support Photovoltaic Module Array. *Sol. Energy* **2024**, *284*, 113096. [CrossRef]
29. Zhou, Y.; Peng, R.; Xiang, Y.; Li, M.; Xi, G.; Li, Y.; Luo, N. Experimental Investigation on Wind Loads and Wind-Induced Responses of Large-Span Flexible Photovoltaic Support Structure. *Eng. Struct.* **2025**, *322*, 119009. [CrossRef]
30. Zhou, Y.; Xiang, Y.; Wang, W.; Zhao, J.; Yang, K.; Zhang, Y.; Li, M. Experimental Study on Wind-Induced Response on a 45 m Span Double-Layer Cable-Supported Photovoltaic Structure. *J. Wind Eng. Ind. Aerodyn.* **2025**, *266*, 106213. [CrossRef]
31. Kim, Y.; Tamura, Y.; Yoshida, A.; Ito, T.; Shan, W.; Yang, Q. Experimental Investigation of Aerodynamic Vibrations of Solar Wing System. *Adv. Struct. Eng.* **2018**, *21*, 2217–2226. [CrossRef]
32. Xu, A.; Ma, W.; Yang, W.; Li, M.; Tan, Y.; Zou, C.; Qiang, S. Study on the Wind Load and Wind-Induced Interference Effect of Photovoltaic (PV) Arrays on Two-Dimensional Hillsides. *Sol. Energy* **2024**, *278*, 112790. [CrossRef]
33. Yao, J.; Tu, Z.; Xu, H. Experimental Investigation of Wind Pressures on Photovoltaic (PV) Array Mounted on a Hilly Terrain. *Sol. Energy* **2025**, *291*, 113256. [CrossRef]

34. Barnes, M.R. Form Finding and Analysis of Tension Structures by Dynamic Relaxation. *Int. J. Space Struct.* **1999**, *14*, 89–104. [CrossRef]
35. Yang, Y.B.; Tsay, J.Y. Geometric Nonlinear Analysis of Cable Structures with a Two-Node Cable Element. *Int. J. Struct. Stab. Dyn.* **2007**, *7*, 571–588. [CrossRef]
36. Zhou, R.; Xu, Z.; Wang, H. Parametric Study on Flutter Performance of Three-Cable-Supported Flexible Photovoltaic Support Structure. *Thin-Walled Struct.* **2025**, *210*, 112975. [CrossRef]
37. Abad, M.S.A.; Shooshtari, A.; Esmaeili, V.; Riabi, A.N. Nonlinear Analysis of Cable Structures under General Loadings. *Finite Elem. Anal. Des.* **2013**, *73*, 11–19. [CrossRef]
38. Desai, Y.; Popplewell, N.; Shah, A.; Buragohain, D. Geometric Nonlinear Static Analysis of Cable Supported Structures. *Comput. Struct.* **1988**, *29*, 1001–1009. [CrossRef]
39. *NB/T 10115—2018*; Energy Administration of the People's Republic of China. Structural Design Code for Photovoltaic Supports. China Electric Power Press: Beijing, China, 2018.
40. *T/CSEE 0394—2023*; China Society for Electrical Engineering. Code for Structural Design of Flexible Photovoltaic Supports. China Society for Electrical Engineering: Beijing, China, 2023.

Disclaimer/Publisher's Note: The statements, opinions and data contained in all publications are solely those of the individual author(s) and contributor(s) and not of MDPI and/or the editor(s). MDPI and/or the editor(s) disclaim responsibility for any injury to people or property resulting from any ideas, methods, instructions or products referred to in the content.